# HSA-MnO$_2$-$^{131}$I Combined Imaging and Treatment of Anaplastic Thyroid Carcinoma

**Ziyu Yan, MD[1],\***, **Xuemei Zhang, MD[1],\***, **Yifan Liu, MM[2]**,
**Yiming Shen, MD[1]**, **Ning Li, PhD[1]**, **Qiang Jia, MD[1]**, **Yanhui Ji, MD[1]**,
**Peitao Zhang, PhD[2]**, **Li Zhao, PhD[2]**, and **Zhaowei Meng, MD, PhD[1]** iD

## Abstract

**Purpose** Compelling evidence suggests that nanoparticles (NPs) play a crucial role in cancer therapy. NPs templated with human serum albumin (HSA) has good retention in tumors. Manganese dioxide (MnO$_2$) has been used to enhance the effect of radiotherapy. In this study, synthesized NPs using HSA-MnO$_2$ labeled $^{131}$I to perform both imaging and therapy for anaplastic thyroid carcinoma (ATC). **Method** HSA-MnO$_2$ was synthesized via HSA using a simple biomineralization method, and then labeled with Na$^{131}$I by the chloramine T method. The cytotoxicity and biosafety of HSA-MnO$_2$ were evaluated by the MTT test. The proliferation-inhibiting effect of HSA-MnO$_2$-$^{131}$I was evaluated in papillary thyroid cancer cell lines (K1, BCPAP, and KTC) and anaplastic thyroid carcinoma cell lines (Cal62, THJ16T, and ARO). For further translational application in medicine, we established a model of transplantable subcutaneously tumors in BALB\c-nu mice to assess the anti-tumor effect of HSA-MnO$_2$-$^{131}$I. The imaging effects of NPs were evaluated by MRI and SPECT/CT. **Results** The MTT test proved that the HSA-MnO$_2$ had low toxicity. HSA-MnO$_2$-$^{131}$I significantly inhibited the proliferation of PTC and ATC cell lines. In addition, the results unveiled that HSA-MnO$_2$-$^{131}$I exhibited dual-modality MR/SPECT imaging for thyroid cancer visualization. In particular, HSA-MnO$_2$-$^{131}$I had an enhanced T1 signal in MR. Using SPECT/CT, we observed that HSA-MnO$_2$-$^{131}$I had good retention in tumor tissue, which was helpful for the diagnosis and treatment of tumor. *In vivo* assays indicated that the NPs led to a reduction in radioresistance in the tumor hypoxic microenvironment. **Conclusion** The nanomaterial had a simple synthesis method, good water solubility and biosafety, and good retention in tumor tissue. Hence, it could be used for SPECT/CT and MR dual mode imaging and therapy with radioiodine of tumor cells. The experimental results provided a feasible solution for combining radiotherapy and dual-model imaging by NPs for cancer diagnosis and treatment.

## Keywords

nanomaterials, radioiodine, combination therapy, proliferation

## Abbreviations

RT, radiation therapy; MRI, magnetic resonance imaging; HSA, human serum albumin; MnCl$_2$, manganese dichloride; NaOH, sodium hydroxide; DMEM, Dulbecco's modified Eagle medium; PBS, phosphate-buffered saline; FBS, fetal bovine serum; DMSO, dimethyl sulfoxide; ATC, anaplastic thyroid carcinoma; MTT, 3-(4,5-dimethylthiazol-2-yl)-2,5-diphenyltetrazolium bromide; AM, calcein-acetoxymethyl; PI, propidium iodide; SLC9A1, solute carrier family 9A1; HIF-1$\alpha$, hypoxia inducible factor-1$\alpha$

## Background

The incidence of thyroid cancer has increased considerably in recent years.[1,2] The incidence rate is higher in urban areas of China, especially among women.[3,4] The current treatment methods for thyroid cancer are mainly surgery to remove the tumor and postoperative radioiodine therapy.[5–7] Compared with external radiotherapy, therapy with radioiodine has many obvious advantages. Radiation therapy (RT) is used to evaluate

[1] Department of Nuclear Medicine, Tianjin Medical University General Hospital, Tianjin, P. R. China
[2] Department of Biochemistry and Molecular Biology, School of Basic Medical Sciences, Tianjin Medical University, Tianjin, China

*As co-first authors, contributed equally in this paper.

**Corresponding Author:**
Zhaowei Meng, Department of Nuclear Medicine, Tianjin Medical University General Hospital, Anshan Road No. 154, Heping District, Tianjin 300052, China.
Email: zmeng@tmu.edu.cn

the uptake and retention of the tumor in advance through tracer imaging and select the optimal radiation dose, thus having a significant effect on the treatment of primary and secondary tumors, local lymph node metastasis, and distant metastasis.

In the era of precision medicine, nanomaterials have been extensively investigated as medical reagents, owing to its special physical and chemical properties, such as high permeability, high reactivity, small size, large surface area, and excellent quantum properties. Nanomaterials are widely used in biological sciences and medicine, including drug loading, imaging, disease monitoring, probes, and sensing. Metal nanoparticles (NPs) enhance the therapeutic effect through radiosensitization and synergistic effect in radiotherapy.[8] Efficient delivery of nanosystems reduced drug concentration, thereby reducing fibrosis, soft tissue necrosis, nerve damage, and other side effects.[9,10] $MnO_2$, which has been effectively used in tumor imaging and therapy, is a nanomaterial that has shown promising features appropriate for a wide range of applications. Hypoxia is a major obstacle to cancer treatment. As a kind of redox reaction catalyst, $MnO_2$ reacts with tumor endogenous substances to produce oxygen and improve hypoxia. $MnO_2$ offer metalions that can be used for magnetic resonance imaging (MRI) to obtain more comprehensive information of the tumor structure and pathology for diagnosis.

Therefore, we proposed a new nanotechnology strategy using multi-functional nanomaterials to concentrate the radiation energy and improve the oxygenation of the tumor. The findings suggested that nanomaterials enhanced RT induction during cancer treatment.

## Materials and Methods

### Materials

Human serum albumin (HSA) was purchased from Dingguo Changsheng Biotechnology Co. Ltd (Beijing, China). Manganese dichloride ($MnCl_2$) was purchased from Merck Millpore Company. Sodium hydroxide (NaOH) was purchased from China National Pharmaceutical Group Co., Ltd (Sinopharm, Tianjin, China). 0.9% sodium chloride injection was purchased from Otsuka Pharmaceutical. Sodium iodide were purchased from Fengchuan Chemical Reagent Technology (Tianjin, China). Trypsin digestion solution Dulbecco's modified Eagle medium (DMEM) and penicillin-streptomycin were from Hai Klonn Biochemical (USA). Potassium bromide was purchased from Sigma. Phosphate-buffered saline (PBS) was purchased from Solarbio. Fetal bovine serum (FBS) was purchased from M&C. Dimethyl sulfoxide (DMSO) was obtained from Beijing Solarbio Science & Technology Co., Ltd (Beijing, China). 3-(4,5-dimethylthiazol-2-yl)-2,5-diphenyltetrazolium bromide (MTT) was obtained from SDN. Calcein-acetoxymethyl (AM) and propidium iodide (PI) were purchased from Dongren Chemical Technology (Shanghai, China). Ultrapure water was used for all experiments. All reagents and chemicals used were of analytical grade. SPECT Discovery 670 was purchased from General Electric. The Fourier Transform-Infrared Spectrometer AVATAR-360 was purchased from Nicolli, USA. The MRI definition is from Siemens. The nude mice were obtained from the China Food and Drug Control Institute.

### Synthesis of HSA-MnO₂-¹³¹I, HSA-MnO₂, HSA-¹³¹I, and HSA-MnO₂-¹³¹I-ICG

The HSA-templated $MnO_2$ NPs were prepared using a biotemplate method.[11,12] Manganese chloride ($MnCl_2$) (0.1 M, 1 mL) was slowly added to 50 mg of HSA solution (25 mg/mL, 2 mL) dissolved in 2 mL of water with strong stirring. Then, 350 µL of NaOH (1M) was added to the above solution quickly, and the pH was adjusted to 10 using a pH test paper. The mixture was stirred vigorously for 2 h without sealing at room temperature to obtain a clear solution. HSA-$MnO_2$ was purified by dialysis in distilled water for 48 h to remove excess precursor (membrane molecular weight cut off: 8000-14000), followed by freeze-drying.

HSA-$MnO_2$ (50 mg/mL, 1 mL) dissolved in PBS (0.01 M, pH = 7.4). The I-labeled NPs were synthesized according to a previous study.[13] Chloramine T (5 mg/mL, 1 mL) was dissolved in PBS. $NaI.2H_2O$ (5 mg/mL, 1 mL) was dissolved in water. They were mixed and stirred for 10 min. The reaction was terminated by adding sodium pyrosulfite solution (5 mg/mL, 1 mL).The mixture was purified by ultrafiltration centrifugation several times. HSA-¹³¹I and HSA-$MnO_2$-¹³¹I were prepared using the same method as above, except $NaI.2H_2O$ was replaced with ¹³¹I. HSA-$MnO_2$-¹³¹I-ICG was prepared by HSA-$MnO_2$-¹³¹I and ICG and was mixed and stirred for 2 h. After that, the NPs were centrifuged and washed several times.

### Characterization of NPs

The NP solution was diluted and dropped on the copper mesh. Then, the size of HSA-$MnO_2$ and HSA-$MnO_2$-I was recorded under a transmission electron microscope (TEM). The fluorescence spectra of HSA in different pH solutions were recorded. The experimental details were published in a previous study.[14] The dynamic hydrodynamic diameter and zeta potential of HSA-$MnO_2$ and HSA-$MnO_2$-I were analyzed by a Nano-Zetasizer. The sample was mixed with pure potassium bromide solid (1:200). Fourier transform-infrared spectrometer were recorded.

### Cytotoxicity Assay of HSA-MnO₂

Nthy cells were seeded in a 96-well plate at a density of $1 \times 10^4$. Different concentrations of HSA-$MnO_2$ were prepared, mixed, and incubated in a constant temperature incubator at 37 °C for 24 h. Cells were washed with PBS until there is no material color. Cells were incubated with 10 µL of MTT (5 mg/mL) and 190 µL of medium for 4 h, and the supernatant was washed off with PBS to avoid destroying the purple precipitate

at the bottom. Then, DMSO (150 µL/well) was added, and the the absorbance of each well was measured at 490 nm using a microplate reader. The cell viability was calculated according to the following formula:

Cell viability $= OD_{exp}/OD_{con} \times 100\%$

Where $OD_{exp}$ is the absorbance (OD) at 490 nm of the experimental group of cells with different concentrations of nanomesh after treatment. $OD_{con}$ is the absorbance (OD) at 490 nm after treatment of blank control cells.

## In Vitro Combination Therapy of HSA-MnO$_2$ and HSA-MnO$_2$-$^{131}$I

For evaluating all types of thyroid cancer cells, K1, BCPAP, KTC, Cal62, THJ16T, and ARO cells were incubated in 96-well plates at a density of $1 \times 10^4$ for 24 h. Then, the cells were treated with different concentrations of HSA-$^{131}$I and HSA-MnO$_2$-$^{131}$I for 24 h. Then, 10 µL of MTT (5 mg/mL) and 190 µL of culture medium were added to the cells. After incubating for 4 h, the supernatant was washed with PBS, followed by the addition of DMSO (150 µL/well). After gently shaking on a shaker at low speed for 10 min, the purple precipitate was completely dissolved, and the absorbance was measured at 490 nm.

To evaluate the uptake ability of cells for HSA-MnO$_2$-$^{131}$I, cell climbing pieces were used. Then, Cal62, THJ16T, and ARO cells were incubated with HSA-MnO$_2$-$^{131}$I-ICG for 6 h. Subsequently, the nucleus was stained with DAPI and photographed under a fluorescence microscope.

ARO cells were incubated in a 96-well plate at a density of $1 \times 10^4$ for 24 h. Then, the cells were washed with PBS, treated with HSA-$^{131}$I, HSA-MnO$_2$-$^{131}$I, HSA-MnO$_2$, $^{131}$I, and co-cultured for 12 h. The HSA-MnO$_2$-$^{131}$I group was further incubated for 24 h. Then, cells were stained with AM and PI and incubated for 15 min. Then, cells were visualized under an inverted fluorescence microscope.

## Construction of Animal Models

ARO cells ($2 \times 10^6$) were injected on the right back of the hind legs of 5-week-old BALB\c-nu mice (14-17 g) to construct a moderately sized tumor (about 0.4 cm in diameter).

## In Vivo Imaging by SPECT/CT

The tumor-bearing mice were randomly divided into two groups, with three in each group. Then, mice were intratumorally injected with HSA-MnO$_2$-$^{131}$I and $^{131}$I (100 µL, 37 MBq).

## In Vivo Imaging by MR

Different concentrations of HSA-MnO$_2$-$^{131}$I were added in a centrifuge tube, which was placed upside down on a cardboard for T1 signal acquisition. Subsequently, HSA-MnO$_2$-$^{131}$I (1000 µg/mL, 50 µL) was intratumorally injected into the mice. MR imaging spectra were acquired at different time points.

## In Vivo Therapy with HSA-MnO$_2$-$^{131}$I

The tumor-bearing mice were randomly divided into five groups (A-E), each containing three mice. Subsequently, subjected to the following treatments: (A) intratumoral injection of PBS (100 µL); (B) intratumoral injection of HSA-MnO$_2$ (100 µL, 37 MBq); (C) intratumoral injection of Na$^{131}$I (100 µL, 37 MBq); (D) intratumoral injection of HSA-$^{131}$I (100 µL, 37 MBq); (E) intratumoral injection of HSA-MnO$_2$-$^{131}$I (100 µL, 37 MBq). At different time points, the mouse body weight and tumor size (record the length, width, height, and diameter) were recorded and imaged. On day 26, the five groups of mice were sacrificed, and tumor volumes were measured. To determine the expression level of hypoxia inducible factor-1α (HIF-1α), total protein extracted from tumor tissue was subjected to western blotting.

## In Vivo Safety Assessment

The mice were intravenously injected with PBS and HSA-MnO$_2$-I (100 µL). After 20 days, blood serum was collected for evaluation of liver and kidney function, and the major organs (heart, liver, spleen, lung, and kidney) were harvested for hematoxylin and eosin (HE) staining.

## Statistical Analysis

Data are expressed as the mean ± standard deviation (SD). Differences between groups were analyzed using a two-tailed *t*-test or one-way ANOVA analysis. Values with $P < .05$ were considered statistically significant.

## Results

### Characterization of HSA-MnO$_2$

HSA-MnO$_2$ was prepared by simple biomineralization reactions (Figure 1). HSA-MnO$_2$ had a relatively uniform and suitable particle size, as observed in TEM images (Figure 2A). Through fluorescence spectroscopy, we observed the absorption peak of tryptophan in HSA, which confirmed the stability of HSA under synthesis conditions (Figure 2B). The infrared spectrum of HSA showed many amide bands, which represented different vibrations of peptide bonds (Figure 2C). We observed that HSA-MnO$_2$ had the same absorption peak as HSA. In the HSA-MnO$_2$ spectrum, the hydroxyl bands (at 3282 cm$^{-1}$), amide I (expressed as the stretching vibration of carbonyl C $=$ O at 1644 cm$^{-1}$), and amide II (combination of CN stretching vibration and NH deformation vibration at 1532 cm$^{-1}$) corresponded to the characteristic bands in HSA. Therefore, the presence of HSA was confirmed in the NPs. The hydrodynamics of NPs was studied by DLS (Figure 2D and E). Zetapotential measurements showed that NPs were negatively charged in both PBS and 1640, which could be beneficial for dispersion (Figure 2F). The suitable
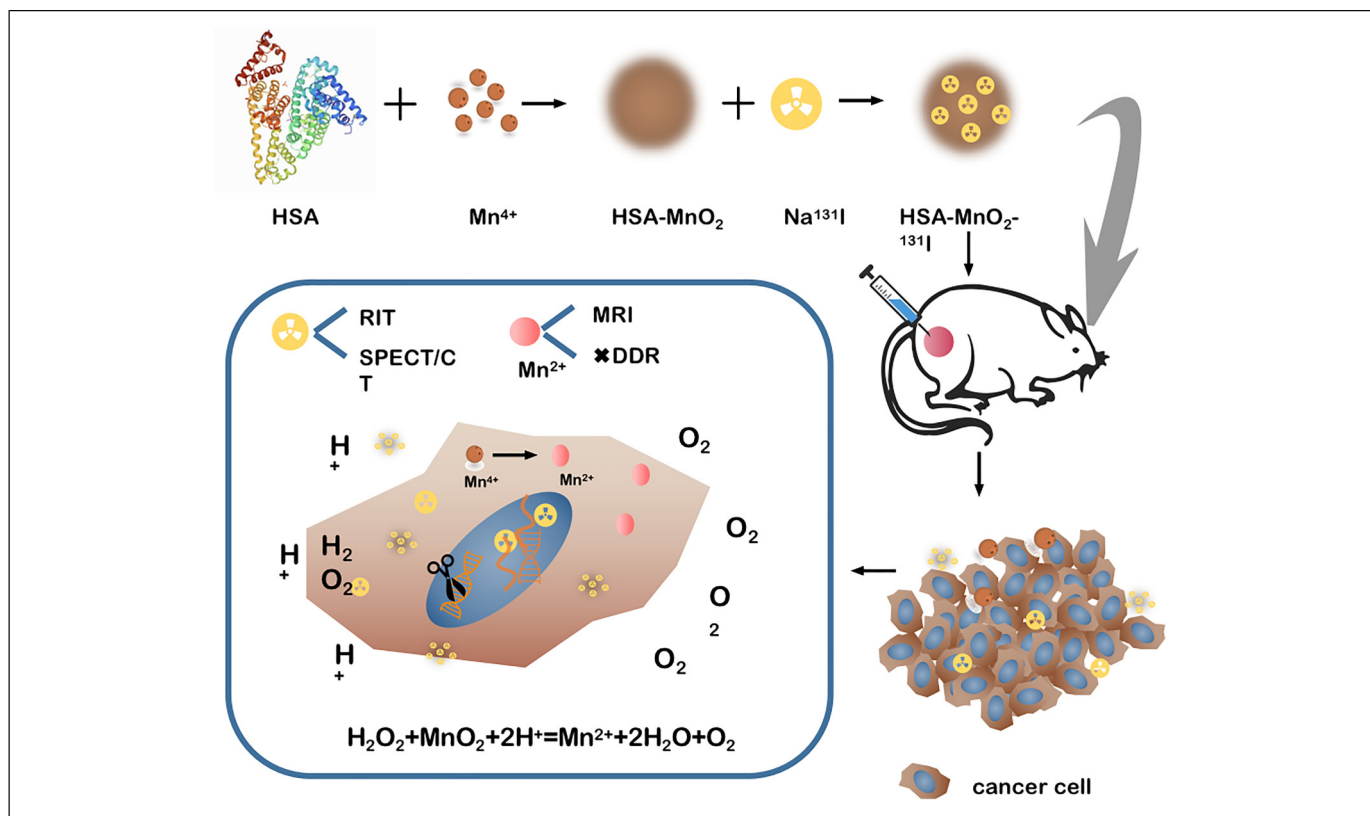
**Figure 1.** Schematic illustration of the nanoparticles HSA-MnO$_2$-$^{131}$I for SPECT/CT/MR imaging and RIT to improved the tumor hypoxic microenvironment.

size and zeta potential was helpful to increase the water solubility and stability of NPs. In different solutions (water, PBS, FBS, and 1640), the NPs were stably dispersed for 30 days without settling. (Figure 2G).

## Cytotoxicity Assay of HSA-MnO$_2$

We evaluated the expression levels of solute carrier family 9A1 (SLC9A1) and HIF-1α in tumor tissues in The Cancer Genome Atlas (TCGA) database to confirm the existence of an acidic and hypoxic microenvironment in thyroid cancer (Figure 3A). SLC9A1 is the most common isoform of the Na$^+$/H$^+$ exchanger family ubiquitously present in all mammalian cells and plays a role in promoting tumor cell motility, invasion, proliferation, growth, and evasion of chemotherapeutic cell death. HIF-1α affects the energy metabolism, proliferation, and apoptosis of tumor cells by participating in the transcriptional regulation of various target genes, causing cells and tissues to produce a series of responses to adapt to the hypoxic environment, eventually increasing the resistance to radiotherapy. The high expression of HIF-1α and SLC9A1 confirmed the hypoxic and acidic microenvironment of thyroid cancer. Hence, this environment was mimicked in the therapeutic system used in the current study.

The MTT assay was used to test the cell cytotoxicity of HSA-MnO$_2$. We showed that the viability of normal thyroid

cells incubated with different concentrations of HSA-MnO$_2$ was more than 75%, even at 2000 µg/mL (Figure 3B). The increased cell survival rate showed that HSA-MnO$_2$ was more safe, allowing for an effective imaging and therapy of cancer.

## In Vitro Combination Therapy of HSA-MnO$_2$ and HSA-MnO$_2$-$^{131}$I

To evaluate the effect of HSA-MnO$_2$-$^{131}$I on the radiosensitivity of tumor cells, we assessed the viability of different types of thyroid cancer cells under different concentration gradients of HSA-MnO$_2$-$^{131}$I and HSA-$^{131}$I (Figure 3C-H). We used PTC (K1, BCPAP, and KTC) and ATC (Cal62, THJ16T, and ARO) cell lines. Under the concentration gradient of HSA-MnO$_2$-$^{131}$I and HSA-$^{131}$I (0-1000 µCi/mL), the cell survival rates were significantly different under the two conditions; the cell survival rate was lower under the HSA-MnO$_2$-$^{131}$I condition than that under the HSA-$^{131}$I condition. The malignancy and radiation resistance of ATC cells were higher than those of PTC cells. Interestingly, HSA-MnO$_2$-$^{131}$I also exerted significant therapeutic effects on ATC cell lines. Based on the above findings, we showed that HSA-MnO$_2$-$^{131}$I was more cytotoxic to thyroid cancer cells than HSA-$^{131}$I.

We demonstrated that HSA-MnO$_2$-$^{131}$I was successfully taken up in anaplastic thyroid cancer cells by examining the
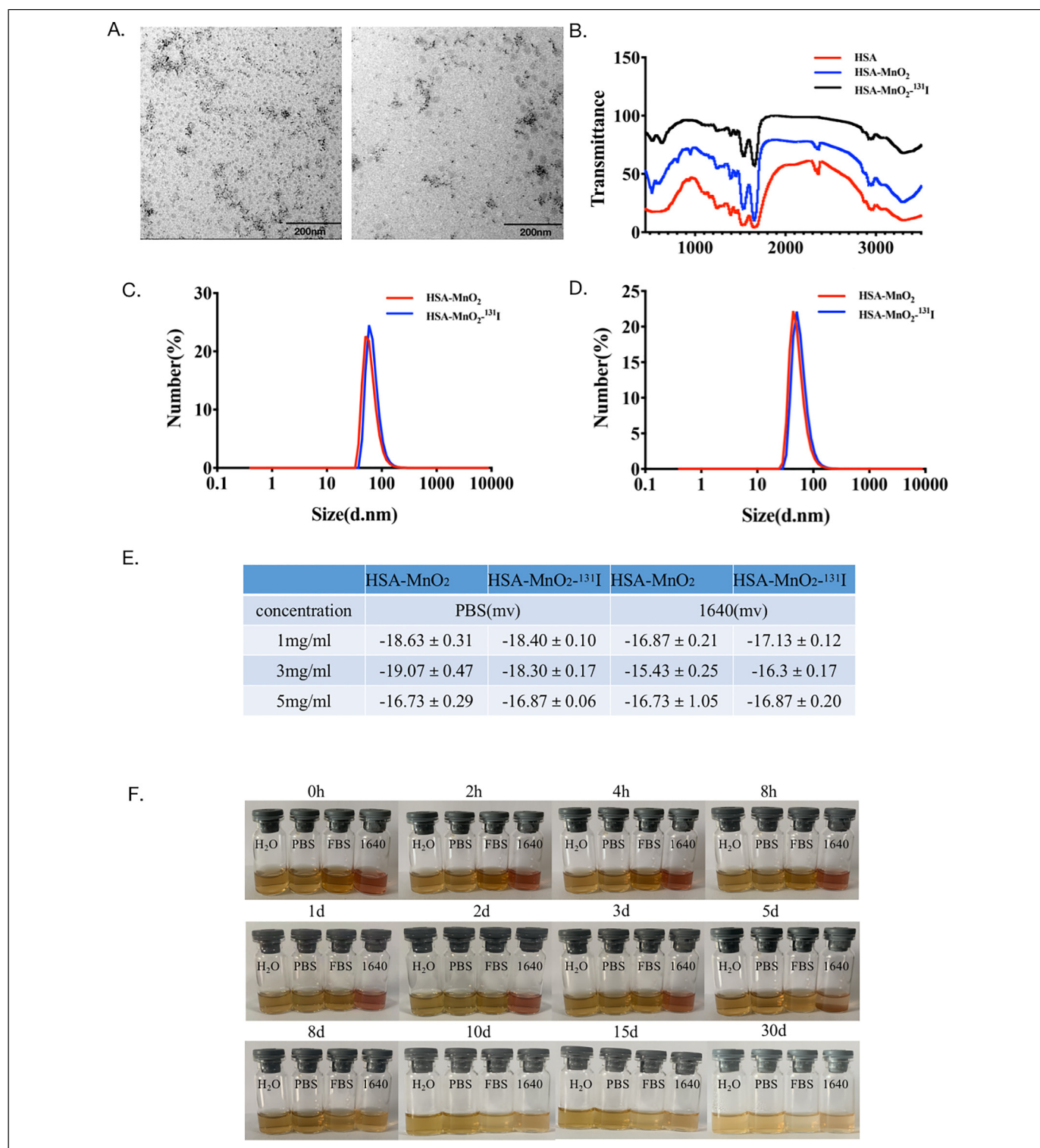
**Figure 2.** Characterization and stability of the nanoparticles. (A) TEM of HSA-MnO$_2$ (left, scale bar = 500 nm) and HSA-MnO$_2$-$^{131}$I (right, scale bar = 500 nm). (B) The fluorescence spectra of HSA in different pH solutions. (C) FT-IR spectra of HSA (red line),HSA-MnO$_2$ (blue line) and HSA-MnO$_2$-$^{131}$I (black line) dispersed in H$_2$O solution. (D) DLS of HSA-MnO$_2$ and HSA-MnO$_2$-$^{131}$I dispersed in aqueous solution. (E) DLS of HSA-MnO$_2$ and HSA-MnO$_2$-$^{131}$I dispersed in PBS. (F)Zeta of HSA-MnO$_2$ and HSA-MnO$_2$-$^{131}$I dispersed in H$_2$O and PBS. (G) Stability of HSA-MnO$_2$-$^{131}$I in H$_2$O, PBS, FBS and 1640.
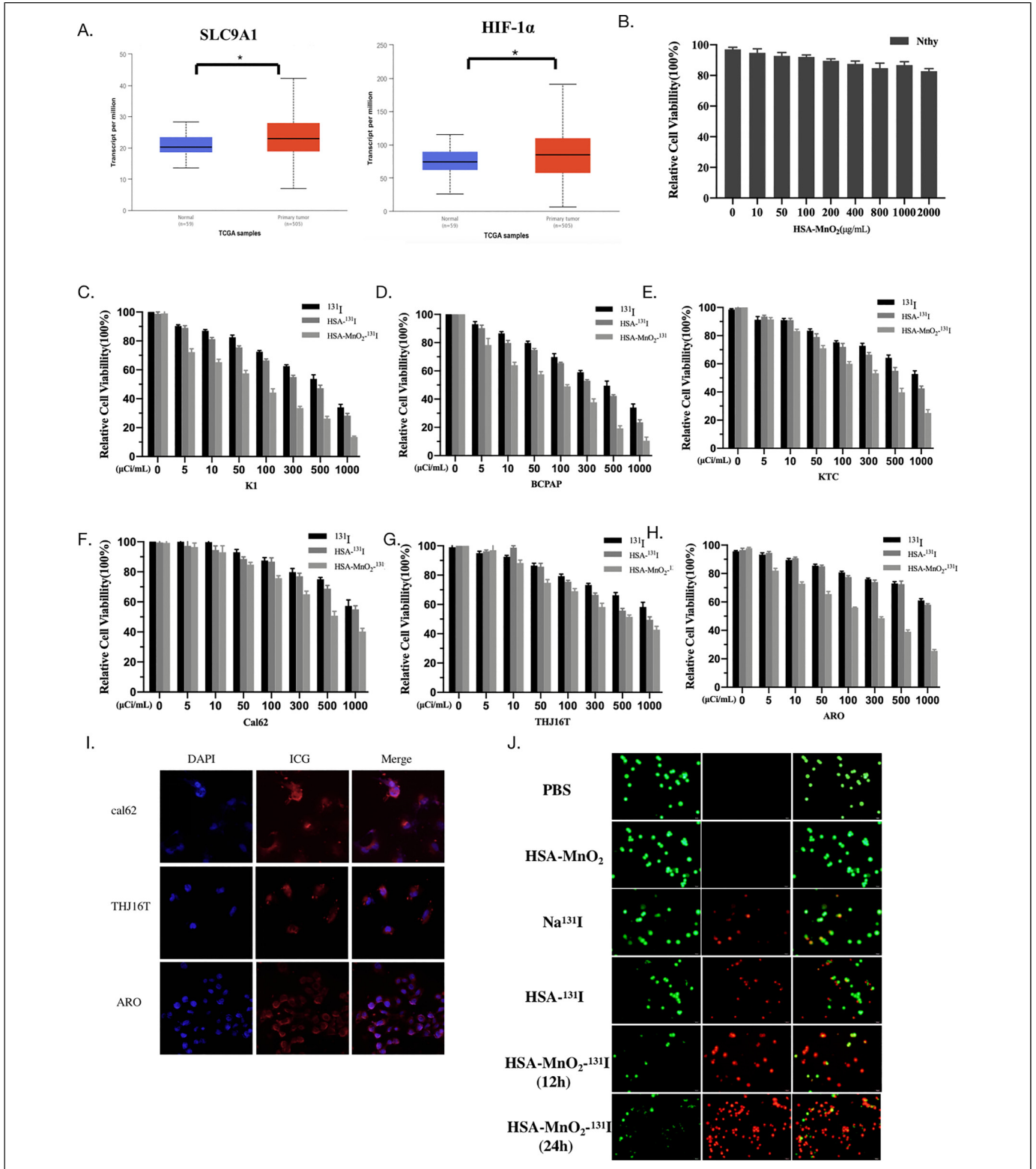
**Figure 3.** HSA-MnO$_2$-$^{131}$I inhibits the proliferation of thyroid cancer cell lines. (A) The expression of SLC9A1 and HIF-1a about PTC and normal tissues in the TCGA dataset. (B) MTT assay using Nthy cells with HSA-MnO$_2$ after 24 h incubation at 37 °C. (C-F) MTT assay using PTC cells (K1,BCPAP and KTC) and ATC cells(Cal62,THJ16T and ARO) with HSA-MnO$_2$ and HSA-MnO$_2$-$^{131}$I after 24 h incubation at 37 °C. (I) Confocal laser scanning microscopy (CLSM) images of ATC cells (Cal62,THJ16T and ARO) after 6 h incubated with HSA-MnO$_2$-$^{131}$I-ICG at 37 °C. (J) Confocal laser scanning microscopy images of ARO cells stained with propidium iodide (PI) and calcein-AM after incubation with different treated (PBS; HSA-MnO$_2$;$^{131}$I;HSA-$^{131}$I;HSA-MnO$_2$-$^{131}$I). Red-channel images show PI staining (535/617 nm), while green-channel images show calcein-AM staining (495/515 nm).

cytoplasmic and nucleus localization of the blue fluorescent signal of DAPI and the red fluorescent signal of ICG (Figure 3I). ATC cell lines lacked the membrane transporter (sodium iodide symporter) possessed by normal thyroid cells, and their $^{131}I$ uptake efficiency was significantly reduced. However, HSA-MnO$_2$-$^{131}I$ was taken up by ATC cell lines via endocytosis/exocytosis. Thus, the therapeutic effect of the radionuclide for ATC was significantly improved.

We performed a fluorescence labeling experiment of live/dead cells to assess the differences between tumor cells in various experimental groups. The results showed that the survival rates of the cells in the PBS and HSA-MnO$_2$ groups were very high (almost all survived). The HSA-MnO$_2$-$^{131}I$ group had a significant killing effect that was higher than that of the free-$^{131}I$ and HSA-$^{131}I$ groups (Figure 3I). When the culture time was extended to 24 h, the number of dead cells grew even more, and the rate of cell survival dropped dramatically. The HSA-MnO$_2$-$^{131}I$ group had a significantly different inhibitory impact on tumor cells than the control group. Radiosensitization of tumor cells occurred in the HSA-MnO$_2$-$^{131}I$ group, which boosted its therapeutic efficacy.

## In Vivo Imaging by SPECT/CT

To observe the retention of radionuclides in mice, we performed HSA-MnO$_2$-$^{131}I$ and free-$^{131}I$ *in vivo* SPECT imaging in mice. The nuclides of the free-$^{131}I$ group were rapidly metabolized, and the HSA-MnO$_2$-$^{131}I$ was highly aggregated in the tumor (Figure 4A). On day 5, the $^{131}I$ group had no obvious accumulation of nuclides. A substantial radioactive buildup was also identified in the tumor region in the HSA-MnO$_2$-$^{131}I$ group. HSA-MnO$_2$-$^{131}I$ was shown to have improved bioavailability and biodistribution.

## MR Imaging of HSA-MnO$_2$-$^{131}I$

Through the T1 signal of HSA-MnO$_2$-$^{131}I$ in different concentrations *in vitro*, the concentration of nanomaterials increased, and the T1 signal also increased (Figure 4B). MR imaging was performed on mice pre-and post-injection. The results showed that the T1 signal at the tumor gradually increased over time. HSA-MnO$_2$-$^{131}I$ disintegrated slowly due to numerous proteases in the tumor site, low pH, and high H2O2 levels in the tumor microenvironment. It promoted the release of Mn$^{2+}$, thereby gradually enhancing the T1-weighted imaging of the tumor. MR imaging facilitated the anatomical sites of HSA-MnO$_2$-$^{131}I$ accumulation in the tumor.

## In Vivo Therapy

Next, we studied the therapeutic effect of HSA-MnO$_2$-$^{131}I$ through *in vivo* experiments. We observed the changes in the tumor volume of mice (Figure 5A, C and D). When compared to other groups, the tumors in the HSA-MnO$_2$-$^{131}I$ group shrank dramatically. The tumor volume grew the most in the PBS group, but it also increased in the free-$^{131}I$ and HSA-MnO$_2$

groups. The results indicated that the free-$^{131}I$ group and HSA-MnO$_2$ group were not effective in inhibiting tumor proliferation. The HSA-MnO$_2$-$^{131}I$ group has a significant improvement in the tumor hypoxic environment and reduction of radioresistance. The weight of the mice in the PBS group and HSA-MnO$_2$ group increased significantly in the first 7 days, which may be due to the rapid growth of the tumor (Figure 5B). The weight of mice in HSA-$^{131}I$, free-$^{131}I$, and HSA-MnO$_2$-$^{131}I$ groups decreased in the early stage, which may be due to the therapeutic effect of radiotherapy on tumor sites. The body weight of the mice in the HSA-MnO$_2$-$^{131}I$ group was relatively stable. Results of western blotting showed that HIF-1α level was significantly downregulated in the mouse tumor tissue, thus confirming that the hypoxic microenvironment of the tumor tissue was reversed by NP treatment (Figure 5E). Compared to the control, treatment with HSA-MnO$_2$ did not significantly affect liver and renal functions, which were within the normal reference value range (Figure 5F). The results of HE staining showed no pathological changes in the main organs (Figure 5G). Moreover, the nanomaterials showed good biocompatibility and negligible biological toxicity. In summary, we confirmed that the HSA-MnO$_2$-$^{131}I$ group had the most excellent therapeutic effect.

## Discussion

The nanomaterial, which was synthesized using a simple method, had good water solubility and biosafety, as well as good retention in tumor tissue. It is commonly recognized that people with thyroid cancer differ from one another. Thyroid cancer is associated with a high level of intratumoral heterogeneity, which is the foundation of tumor cell survival. This is also the primary cause of tumor cell radiation resistance and a major obstacle to improving patient outcomes. Therefore, we selected different types of PTC and ATC cell lines (K1, BCPAP, KTC, Cal62, THJ16T, and ARO cells). The efficiency of nanosystems against ATC cell lines was generally lower than that against PTC cell lines. Our finding is not entirely surprising given that some studies have hypothesized that ATC may be derived from CSCs known as tumor-initiating cells.[15,16] CSCs possess several of the most important cancer cell characteristics, such as self-renewal capacity, resistance to chemotherapy and radiotherapy, multipotency, tumorigenicity, and the ability to recapitulate the heterogeneity of the parent tumor.[17] Therefore, the nanosystem might have had a more significant therapeutic effect on PTC cell lines. Although the killing efficiencies of the different cell lines were slightly different, the killing efficiency of the HSA-MnO$_2$-$^{131}I$ group was significantly different compared to that of the control group. The nanomaterials effectively inhibited the proliferation of PTC and ATC cell lines. Hence, they can be used for SPECT/CT and MR dual mode imaging and therapy with radioiodine of tumor. The experimental results provided a feasible solution for the combination of radiotherapy and dual-model imaging by NPs.
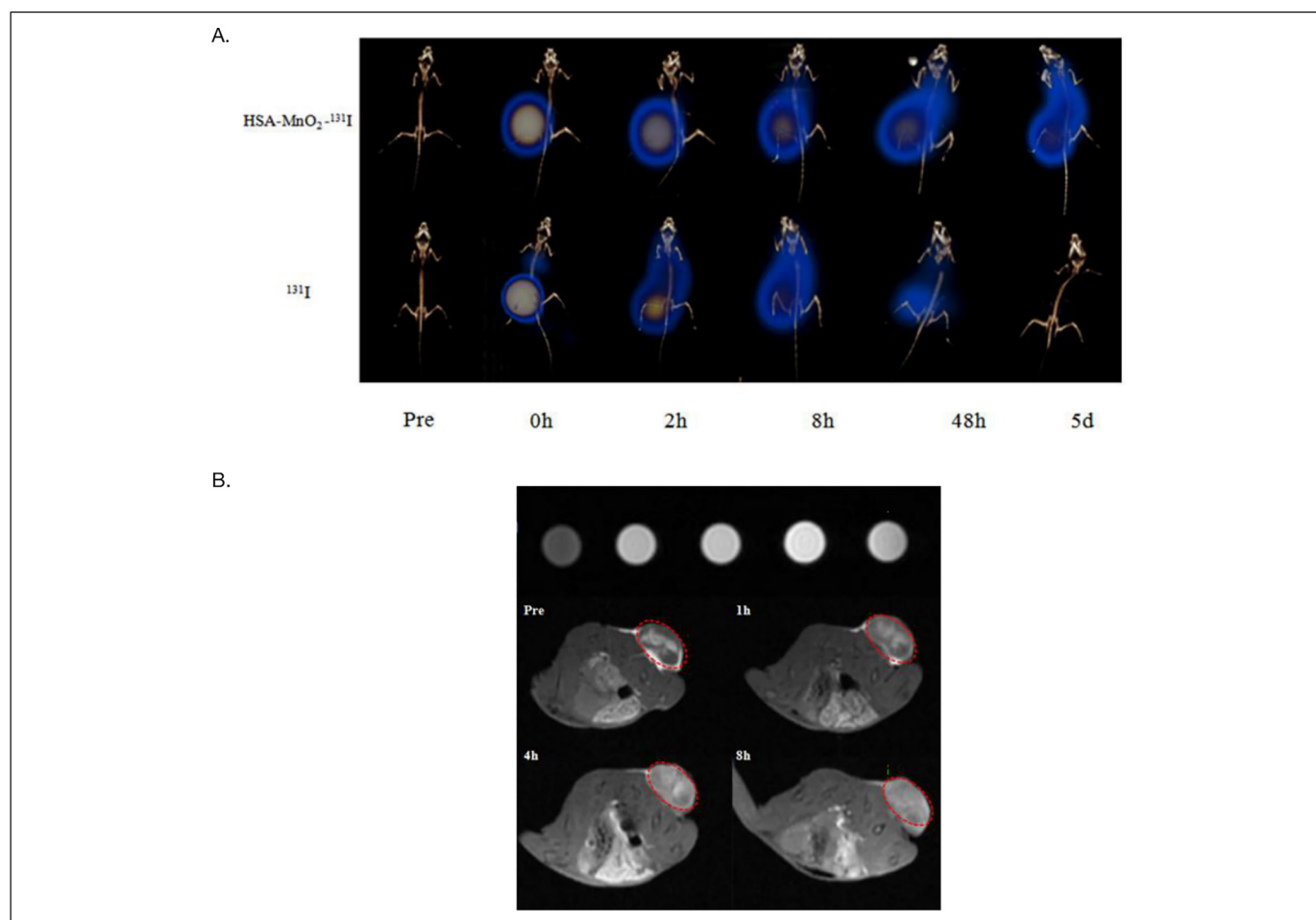
**Figure 4.** HSA-MnO$_2$-$^{131}$I performs dual-modality imaging for tumor diagnosis. (A) SPECT/CT imaging of tumors after situation injection of HSA-MnO$_2$-$^{131}$I. (B) The T1 signal intensity of HSA-MnO$_2$-$^{131}$I was measured in vitro. MR imaging of tumors after situation injection of HSA-MnO$_2$-$^{131}$I.

NPs utilize metals and proteins through biomineralization to form water-soluble metal NPs. Biomineralization produces large amounts of NPs stably and cheaply. NPs have good biological uniformity and water solubility, which can improve cell uptake and reduce biological toxicity. NPs can also be combined with proteins, sugars, and lipids and used for targeted drug delivery.[18] These biomolecules cover the surface of NPs to form a "protein corona".[19] The adsorption layer of proteins modifies the biological characteristics of NPs, which consequently influences their biological behavior. HSA, an important component of plasma, plays an important role in maintaining osmotic pressure balance, transporting, and storing drugs. HSA is a common protein carried on the surface of NPs.[20] Although MnO$_2$ is difficult to dissolve in water, its physical properties can be aletered with the adsorption of protein. Magnetic metals and their compounds have unpaired electrons, which shortens the longitudinal relaxation rate (T1) of protons. This is the reason why they can be used as magnetic resonance contrast agents, especially metal ions with large spin numbers. Manganese has a high spin number, a long relaxation time, and many unpaired electrons, making Mn$^{2+}$ an ideal contrast agent for MRI.

The distribution of drugs and chemical compounds is hampered by an aberrant microenvironment in the tumor, an imbalanced extracellular mechanism, and elevated interstitial fluid pressure.[21] Radioactive nanomaterials are advantageous for cancer imaging because the particle size enhances permeability and retention. It reduces the side effects of radionuclides on normal tissues by improving the efficacy of radiotherapy. The combination of biological properties and multimodal imaging and treatment can be achieved by assembling metal nanomaterials and radionuclides. The therapeutic effect of radionuclide mainly depends on the uptake and residence time of the radionuclide in the tumor. The pharmacokinetics and biodistribution of nanomaterials can be better enhanced. It reduces radiation by improving the accumulation and retention of tumor area. This is beneficial for avoiding normal tissue damage and severe potential renal radiation toxicity.[22]

The integration of radionuclides and nanomaterials creates the imaging and therapeutic characteristics. In an aerobic environment, the radiation sensitivity of cells increases because oxygen can combine with free radicals to form highly stable organic peroxides, leading to permanent damage to the double-
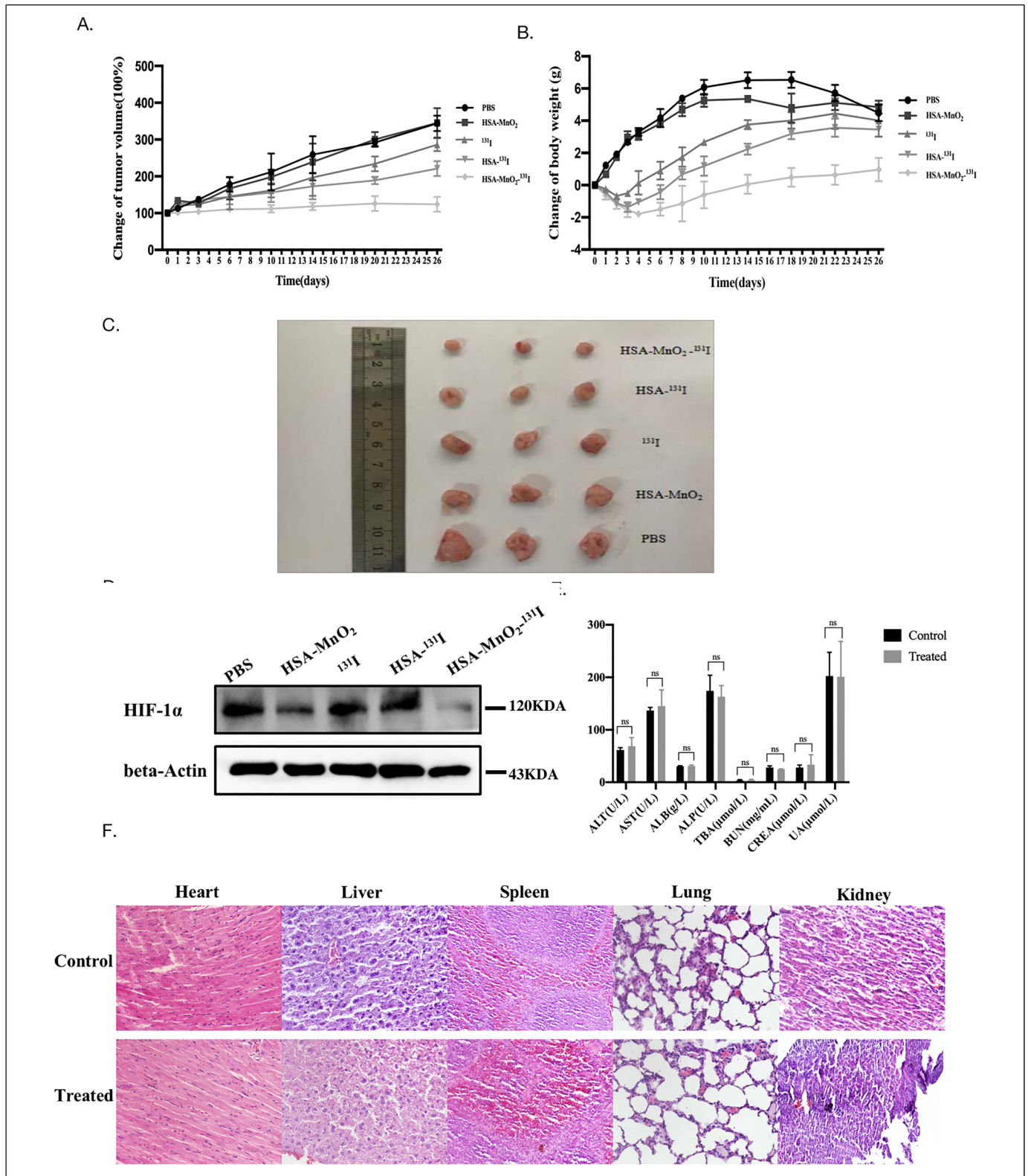
**Figure 5.** Dual therapeutic effects of HSA-MnO$_2$-$^{131}$I in vitro. (A) comparison of tumor volume in each group (n = 3). (B) Body weight change of tumor-bearing mice in each group over 26 days (n = 3). (C) Photos of tumors dissected from each group (n = 5). (D) Expression level of HIF-1a of tumor tissues, (E) The blood levels of ALT, AST, ALB, ALP, TBA, BUN, CREA and UB from injection group and control group. (F) HE staining images of major organs (Heart, Liver, Spleen, Lung and Kidney) of injection group and control group. *P < .05, **P < .001; n.s. represents no significance.

stranded structure of DNA. This mechanism can cause damage to cancer cells including stem cells.[23] However, the tumor microenvironment is not consistent with the condition. The tumor microenvironment is usually characterized by low oxygen levels, acidic conditions, endogenous high levels of $H_2O_2$, and unbalanced nutrient distribution. Hypoxia is a malignant feature of cancer, and tumor cells adapt to the hypoxic state. The microenvironment undergoes a series of physiological changes such as anaerobic energy supply, angiogenesis and metabolic regulation.[24,25] Moreover, it leads to increased radiation resistance and chemotherapy resistance.[26,27] A hypoxic microenvironment increases the chance of tumor occurrence and leads to local tumor infiltration and distant metastasis by accumulation of extracellular adenosine in tumors.[28,29] $MnO_2$ acts as a catalyst to react with the endogenous $H_2O_2$ of the tumor microenvironment and generate $O_2$. It decreases the radiation resistance caused by hypoxia and enhances the sensitivity to ionizing radiation. Furthermore, glutathione can combine with reactive oxygen species. The killing ability of malignant cells induced by radiotherapy depends on the oxygen free radicals produced by ionizing radiation, which can cause irreversible oxidative damage to cancer cells. $MnO_2$ has a clearing effect on glutathione in cells, which may further increase the radiation sensitivity of tumor cells.

Our study had the following limitations. First, we opted for intratumoral injection instead of tail vein injection as the route of administration. We have also tried tail vein injection in the pre-experiment. However, the targeting ability of NPs was relatively poor. Relying on the passive targeting of EPR, it was difficult to treat solid tumors with safe doses of the drugs. In the future, we will try to administer drugs, such as folic acid, peptides and homologous cancer cell membranes, to through tail vein injection for improved targeting. Second, we only chose a single radionuclide.

## Conclusion

In this study, we synthesized HSA-$MnO_2$ NPs using a biomineralization reaction. Furthermore, the chloramine T method was used to label[131]I to form HSA-$MnO_2$-^{131}I, which was was used for imaging and treatment of anaplastic thyroid cancer. Compared with free-^{131}I, HSA-$MnO_2$-^{131}I maximized the accumulation in the tumor area and slowed down the diffusion of radionuclides to improve the therapeutic effect. Based on the results of treatments for anaplastic thyroid cancer models, we confirmed that NPs had good biological safety, retention, and radiosensitization effects. We inferred that protein-modified metal ions and radionuclide have great potential for sensitive tumor detection and specific treatment.

## Authors' Note

All animal experiments were performed according to the protocols and guidelines approved by the Tianjin Medical University Institutional Animal Care and Use Committee (Approval number: TMUaMEC 2019010).

## ORCID iD

Zhaowei Meng [iD] https://orcid.org/0000-0002-4478-878X

## References

1. Lansford CD, Teknos TN. Evaluation of the thyroid nodule. *Cancer Control*. 2006;13(2):89-98.
2. James BC, Mitchell JM, Jeon HD, Vasilottos N, Grogan RH, Aschebrook-Kilfoy B. An update in international trends in incidence rates of thyroid cancer, 1973-2007. *Cancer Causes Control*. 2018;29(4-5):465-473.
3. Yang L, Zheng R, Wang N, Zhang S, Chen W. Analysis of incidence and mortality of thyroid cancer in China, 2010. *Zhonghua Yu Fang Yi Xue Za Zhi*. 2014;48(8):663-668.
4. Yang L, Zheng RS, Wang N, et al. Analysis of incidence and mortality of thyroid cancer in China, 2013. *Zhonghua Zhong Liu Za Zhi*. 2017;39(11):862-867.
5. Mazzaferri EL, Kloos RT. Clinical review 128: current approaches to primary therapy for papillary and follicular thyroid cancer. *J Clin Endocrinol Metab*. 2001;86(4):1447-1463.
6. Willegaignon J, Sapienza M, Ono C, et al. Outpatient radioiodine therapy for thyroid cancer: a safe nuclear medicine procedure. *Clin Nucl Med*. 2011;36(6):440-445.
7. Fard-Esfahani A, Emami-Ardekani A, Fallahi B, et al. Adverse effects of radioactive iodine-131 treatment for differentiated thyroid carcinoma. *Nucl Med Commun*. 2014;35(8):808-817.
8. Howard D, Sebastian S, Le QVC, Thierry B, Kempson I. Chemical mechanisms of nanoparticle radiosensitization and radioprotection: a review of structure-function relationships influencing reactive oxygen species. *Int J Mol Sci*. 2020;21(2):579.
9. Mendes RL, Nutting CM, Harrington KJ. Managing side effects of radiotherapy in head and neck cancer. *Hosp Med*. 2002;63(12):712-717.
10. Wittig A, Engenhart-Cabillic R. Cardiac side effects of conventional and particle radiotherapy in cancer patients. *Herz*. 2011;36(4):311-324.
11. Ren H, Yang Q, Yong J, et al. Mitochondria targeted nanoparticles to generate oxygen and responsive-release of carbon monoxide for enhanced photogas therapy of cancer. *Biomater Sci*. 2021;9(7):2709-2720.

12. Ge J, Cai R, Chen X, et al. Facile approach to prepare HSA-templated $MnO_2$ nanosheets as oxidase mimic for colorimetric detection of glutathione. *Talanta*. 2019;195(Apr 1):40-45.

13. Shaw AK, Pal SK. Spectroscopic studies on the effect of temperature on pH-induced folded states of human serum albumin. *J Photochem Photobiol B*. 2008;90(1):69-77.

14. Li W, Liu Z, Li C, et al. Radionuclide therapy using (1)(3)(1) I-labeled anti-epidermal growth factor receptor-targeted nanoparticles suppresses cancer cell growth caused by EGFR overexpression. *J Cancer Res Clin Oncol*. 2016;142(3):619-632.

15. Takano T. Fetal cell carcinogenesis of the thyroid: A modified theory based on recent evidence [My Opinion]. *Endocrine Journal*. 2014;61(4):311–320. http://dx.doi.org/10.1507/endocrj.EJ13-0517

16. Hardin H, Zhang R, Helein H, Buehler D, Guo Z, Lloyd R V. The evolving concept of cancer stem-like cells in thyroid cancer and other solid tumors. *Laboratory Investigation*. 2017;97(10):1142–1151. http://dx.doi.org/10.1038/labinvest.2017.41

17. Medema JP. Cancer stem cells: The challenges ahead. *Nature Cell Biology*. 2013;15(4):338–344. http://dx.doi.org/10.1038/ncb2717

18. Treuel L, Nienhaus GU. Toward a molecular understanding of nanoparticle-protein interactions. *Biophys Rev*. 2012;4(2):137-147.

19. Shang Li, Nienhaus GU. Metal nanoclusters: Protein corona formation and implications for biological applications. *The International Journal of Biochemistry & Cell Biology*. 2016;75:175–179. http://dx.doi.org/10.1016/j.biocel.2015.09.007

20. Ziegler-Borowska M, Mylkie K, Kozlowska M, et al. Effect of geometrical structure, drying, and synthetic method on aminated chitosan-coated magnetic nanoparticles utility for HSA effective immobilization. *Molecules*. 2019;24(10):1925.

21. Zeng W, Liu P, Pan W, Singh SR, Wei Y. Hypoxia and hypoxia inducible factors in tumor metabolism. *Cancer Lett*. 2015;356(2 Pt A):263-267.

22. Lambert B, Cybulla M, Weiner SM. Renal toxicity after radionuclide therapy. *Radiat Res*. 2004;161(5):607-611.

23. Baumann M, Krause M, Overgaard J, et al. Radiation oncology in the era of precision medicine. *Nat Rev Cancer*. 2016;16(4):234-249.

24. Brown JM, Wilson WR. Exploiting tumour hypoxia in cancer treatment. *Nat Rev Cancer*. 2004;4(6):437-447.

25. Junttila MR, de Sauvage FJ. Influence of tumour microenvironment heterogeneity on therapeutic response. *Nature*. 2013;501(7467):346-354.

26. Nordsmark M, Overgaard M, Overgaard J. Pretreatment oxygenation predicts radiation response in advanced squamous cell carcinoma of the head and neck. *Radiother Oncol*. 1996;41(1):31-39.

27. Aebersold DM, Burri P, Beer KT, et al. Expression of hypoxia-inducible factor-1alpha: a novel predictive and prognostic parameter in the radiotherapy of oropharyngeal cancer. *Cancer Res*. 2001;61(7):2911-2916.

28. Facciabene A, Peng X, Hagemann IS, et al. Tumour hypoxia promotes tolerance and angiogenesis via CCL28 and T(reg) cells. *Nature*. 2011;475(7355):226-230.

29. Hatfield SM, Kjaergaard J, Lukashev D, et al. Immunological mechanisms of the antitumor effects of supplemental oxygenation. *Sci Transl Med*. 2015;7(277):277ra30.